

Research Article

Triangular Wavelets: An Isotropic Image Representation with Hexagonal Symmetry

Kensuke Fujinoki and Oleg V. Vasilyev

Department of Mechanical Engineering, University of Colorado, 427 UCB, Boulder, CO 80309, USA

Correspondence should be addressed to Kensuke Fujinoki, kensuke.fujinoki@gmail.com

Received 19 May 2009; Accepted 14 September 2009

Recommended by James Fowler

This paper introduces triangular wavelets, which are two-dimensional nonseparable biorthogonal wavelets defined on the regular triangular lattice. The construction that we propose is a simple nonseparable extension of one-dimensional interpolating wavelets followed by a straightforward generalization. The resulting three oriented high-pass filters are symmetrically arranged on the lattice, while low-pass filters have hexagonal symmetry, thereby allowing an isotropic image processing in the sense that three detail components are distributed uniformly. Applying the triangular filter to images, we explore applications that truly benefit from the triangular wavelets in comparison with the conventional tensor product transforms.

Copyright © 2009 K. Fujinoki and O. V. Vasilyev. This is an open access article distributed under the Creative Commons Attribution License, which permits unrestricted use, distribution, and reproduction in any medium, provided the original work is properly cited.

1. Introduction

Image processing is one of the most demanded areas of signal processing applications, where the wavelet transform has been offered significant performance advantages [1]. In most cases, the wavelet transform is carried out in the tensor product form, that is, by applying a one-dimensional transform repeatedly in the horizontal and vertical directions. This gives the simple two-dimensional extension of wavelet transforms and yields the lower-resolution images consisting of the approximation and three detail components that contain directional information. In the case of this separable transform, however, the diagonal detail component is only the product of horizontal and vertical details. Thus, isotropy in the sense of uniform distribution of three detail components may not be well respected.

To remedy this drawback many attempts have been carried out to construct nonseparable wavelets [2, 3] or to implement dual-tree complex wavelet transform [4, 5], though the constructions of the associated filters are highly involved and computationally complex. The largest bottleneck is the lack of intrinsically two-dimensional wavelets that are easy to use.

On the other hand, in the framework of subdivision scheme, the wavelet transforms on more general data sets

such as geometric meshes or surfaces have been successfully implemented [6, 7]. In particular, with the advent of lifting scheme [8], the so-called second generation wavelets [9] have opened a way to handle data on irregular grids over arbitrary surfaces [10, 11]. Their main aim is, however, the efficient representation of large data sets and isotropy and/or rotational symmetry in two-dimensional data are not a major concern. If we limit to data on a plane such as images, the usual first generation wavelets would be more desirable, since they would allow more general treatments due to their periodicity on the plane.

In this context a new class of wavelets, called triangular wavelets, whose nonseparable biorthogonal filters are defined on a regular triangular lattice have recently been proposed [12]. Our formulation is based on a straightforward generalization of one-dimensional settings including the lifting. This allows the simple nonseparable extension of biorthogonal wavelets without losing their special properties such as vanishing moments, which are a crucial criterion for both stability and smoothness of wavelets.

In this paper we further develop the triangular wavelets by extending one-dimensional interpolating wavelets to triangular lattice and show a general procedure to generate triangular wavelet filters for any order or any number of vanishing moments. The proposed triangular-lattice wavelets

are expected to improve smoothness characteristics of low-order triangular filters discussed in [13]. In addition we have observed that the energy of decomposed images is evenly distributed over the three detail components. This suggests that the triangular wavelets are promising in keeping isotropy of images, which has been a key issue in wavelet-based image processing.

As an interpolation technique, we use the Lagrange interpolation, which is a standard method of a pointwise polynomial interpolation [14]. Whereas B-splines are also known to have good approximation orders, the Lagrangian method allows us to construct interpolating wavelets having any number of vanishing moments [15]. Unlike in the case of splines, their coefficients are given by easy explicit formulas, and the associate functions are an optimal tradeoff between support size and approximation order, in a similar way to Daubechies wavelets [16]. Moreover, the wavelet transform with any order of the interpolating filters can be implemented by only two lifting steps. This remarkable fact would be quite important in our direct generalization scheme.

It should be noted that orthogonal quadrature mirror filters and biorthogonal wavelets defined on the triangular lattice have also been considered [17–19]. While their formulations partially agree with ours, one of the crucial differences is that their filter construction relies on the numerical analysis technique or algebraic approaches. In contrast, our method uses direct generalization of lifting and, thus, resulting in easy construction of biorthogonal wavelet filters or perfect reconstruction filters. In addition to low computational cost of the triangular wavelet transform, the filter coefficients are all rational numbers.

This paper is organized as follows. Section 2 briefly reviews the one-dimensional wavelets including the lifting scheme and interpolating wavelets. The two-dimensional nonseparable biorthogonal wavelets on triangular lattice are developed in Section 3. The application of triangular wavelet transform to image analysis and performance comparison with conventional tensor product wavelets are given in Section 4. Finally, conclusions are drawn in Section 5.

2. Biorthogonal Wavelets

2.1. Perfect Reconstruction Filters. The wavelet transform decomposes a signal $c_j[k]$, $j, k \in \mathbb{Z}$ into the coarse component $c_{j-1}[k]$ and detail component $d_{j-1}[k]$ by a low-pass (LP) filter $h[k]$ and a high-pass (HP) filter $g[k]$ followed by subsampling. In the Fourier domain, the signal is defined by

$$\hat{c}_j(\omega) = \sum_{k \in \mathbb{Z}} c_j[k] e^{-i\omega k}, \quad \omega \in \mathbb{R}, \quad (1)$$

and the decomposition is written as

$$\begin{pmatrix} \hat{c}_{j-1}(2\omega) \\ \hat{d}_{j-1}(2\omega) \end{pmatrix} = \frac{1}{2} \widehat{M}^*(\omega) \begin{pmatrix} \hat{c}_j(\omega) \\ \hat{c}_j(\omega + \pi) \end{pmatrix}, \quad (2)$$

where $\widehat{M}^*(\omega)$ is the complex conjugate of the modulation matrix

$$\widehat{M}(\omega) = \begin{pmatrix} \hat{h}(\omega) & \hat{h}(\omega + \pi) \\ \hat{g}(\omega) & \hat{g}(\omega + \pi) \end{pmatrix}. \quad (3)$$

Here, we assume that $\hat{h}(0) = \sqrt{2}$ and $\hat{g}(0) = 0$. The reconstruction of the original signal is carried out by taking the reverse steps using the dual filters $\tilde{h}[k]$ and $\tilde{g}[k]$, which may be written as

$$\begin{pmatrix} \hat{c}_j(\omega) \\ \hat{c}_j(\omega + \pi) \end{pmatrix} = \widetilde{M}^T(\omega) \begin{pmatrix} \hat{c}_{j-1}(2\omega) \\ \hat{d}_{j-1}(2\omega) \end{pmatrix}, \quad (4)$$

where $\widetilde{M}(\omega)$ is the transpose of the dual modulation matrix defined similarly as (3). The exact reconstruction of the original signal from the decomposition is guaranteed if the filters satisfy the perfect reconstruction condition

$$\widetilde{M}^T(\omega) \widehat{M}^*(\omega) = 2I. \quad (5)$$

Such particular filters are called perfect reconstruction filters or biorthogonal filters that satisfy the biorthogonality condition derived from (5)

$$\begin{aligned} \hat{h}(\omega) \hat{h}^*(\omega) + \hat{g}(\omega) \hat{g}^*(\omega) &= 2, \\ \hat{h}(\omega) \hat{h}^*(\omega + \pi) + \hat{g}(\omega) \hat{g}^*(\omega + \pi) &= 0, \end{aligned} \quad (6)$$

with

$$\hat{g}(\omega) = e^{-i\omega} \hat{h}^*(\omega + \pi), \quad \hat{g}(\omega) = e^{-i\omega} \hat{h}^*(\omega + \pi). \quad (7)$$

Once a set of biorthogonal filters are devised, the associated scaling functions $\hat{\phi}$ and wavelets $\hat{\psi}$ are defined by

$$\hat{\phi}(\omega) = \frac{1}{\sqrt{2}} \hat{h}\left(\frac{\omega}{2}\right) \hat{\phi}\left(\frac{\omega}{2}\right), \quad \hat{\psi}(\omega) = \frac{1}{\sqrt{2}} \hat{g}\left(\frac{\omega}{2}\right) \hat{\phi}\left(\frac{\omega}{2}\right), \quad (8)$$

whose inverse Fourier transforms yield the particular relations

$$\begin{aligned} \phi(t) &= \sum_{k \in \mathbb{Z}} \sqrt{2} h[k] \phi(2t - k), \\ \psi(t) &= \sum_{k \in \mathbb{Z}} \sqrt{2} g[k] \phi(2t - k). \end{aligned} \quad (9)$$

Their dual functions are also defined by using dual filters in a similar way which, together with the primal pair, turn out to form an biorthogonal basis for $L^2(\mathbb{R})$.

We now move to the polyphase domain to introduce the lifting scheme for construction of biorthogonal wavelet filters. In the polyphase representation, a signal $c_j[k]$ is defined in terms of its even and odd components separately

$$\hat{c}_{j,e}(\omega) = \sum_{k \in \mathbb{Z}} c_j[2k] e^{-i\omega k}, \quad \hat{c}_{j,o}(\omega) = \sum_{k \in \mathbb{Z}} c_j[2k + 1] e^{-i\omega k}. \quad (10)$$

We then have the relation

$$\begin{pmatrix} \hat{c}_j(\omega) \\ \hat{c}_j(\omega + \pi) \end{pmatrix} = \hat{U}(\omega) \begin{pmatrix} \hat{c}_{j,e}(2\omega) \\ \hat{c}_{j,o}(2\omega) \end{pmatrix}, \quad (11)$$

where

$$\hat{U}(\omega) = \begin{pmatrix} 1 & e^{-i\omega} \\ 1 & e^{-i(\omega+\pi)} \end{pmatrix}. \quad (12)$$

With the polyphase form of an LP filter $h[k]$ and an HP filter $g[k]$ defined similarly as (10), we assemble the polyphase matrix as

$$\hat{P}(\omega) = \begin{pmatrix} \hat{h}_e(\omega) & \hat{g}_e(\omega) \\ \hat{h}_o(\omega) & \hat{g}_o(\omega) \end{pmatrix}, \quad (13)$$

so that

$$\hat{P}(2\omega)^\dagger = \frac{1}{2} \hat{M}^*(\omega) \hat{U}(\omega), \quad (14)$$

where $\hat{P}(\omega)^\dagger$ is the Hermitian conjugate of the polyphase matrix. The modulation matrix can also be found from the polyphase matrix

$$\hat{M}^T(\omega) = \hat{U}(\omega) \hat{P}(2\omega). \quad (15)$$

In the polyphase domain, decomposition (2) and the reconstruction (4) may be rewritten as

$$\begin{pmatrix} \hat{c}_{j-1}(\omega) \\ \hat{d}_{j-1}(\omega) \end{pmatrix} = \hat{P}(\omega)^\dagger \begin{pmatrix} \hat{c}_{j,e}(\omega) \\ \hat{c}_{j,o}(\omega) \end{pmatrix}, \quad (16)$$

$$\begin{pmatrix} \hat{c}_{j,e}(\omega) \\ \hat{c}_{j,o}(\omega) \end{pmatrix} = \hat{\tilde{P}}(\omega) \begin{pmatrix} \hat{c}_{j-1}(\omega) \\ \hat{d}_{j-1}(\omega) \end{pmatrix},$$

where $\hat{\tilde{P}}(\omega)$ is the dual polyphase matrix formed similarly as (13) with dual filters \tilde{h} and \tilde{g} . Then the perfect reconstruction condition (5) becomes

$$\hat{\tilde{P}}(\omega) \hat{P}(\omega)^\dagger = I. \quad (17)$$

Thus, finding the perfect reconstruction filters $(h, \tilde{h}, g, \tilde{g})$ amounts to find $\hat{P}(\omega)^\dagger$ and $\hat{\tilde{P}}(\omega)$ that satisfy (17). This condition implies that the matrices must be invertible, and the inverse should be polynomials of $e^{\pm i\omega}$, which provides perfect reconstruction FIR filters and thus compactly supported wavelets.

2.2. Lifting Scheme. Lifting is a convenient method to construct an invertible polyphase matrix. The odd component $c_j[2k+1]$ is predicted by a predictor p using the even component $c_j[2k]$, and $c_j[2k+1]$ is replaced by $d_{j-1}[k]$ which is the differences between the original values and the prediction at the odd indices

$$c_j[2k+1] \rightarrow d_{j-1}[k] = c_j[2k+1] - p(c_j[2k]). \quad (18)$$

The even component $c_j[2k]$ is then updated using the results of the prediction

$$c_j[2k] \rightarrow c_{j-1}[k] = c_j[2k] + u(d_{j-1}[k]), \quad (19)$$

where the updater u is designed so that the coarse signal preserves the average of the original signal

$$\sum_k c_{j-1}[k] = \frac{1}{2} \sum_k c_j[k]. \quad (20)$$

Note the fact that the computation in these two steps can be performed in-place, which reduces computational cost of the wavelet transform. Finally, $c_{j-1}[k]$ and $d_{j-1}[k]$ are scaled by K and $1/K$, respectively, for the energy normalization $\|c_j[k]\|^2 = \|c_{j-1}[k]\|^2 + \|d_{j-1}[k]\|^2$.

Each lifting step corresponds to the factorization of the polyphase matrix

$$\hat{P}(\omega)^\dagger = \begin{pmatrix} K & 0 \\ 0 & \frac{1}{K} \end{pmatrix} \begin{pmatrix} 1 & \hat{u}(\omega) \\ 0 & 1 \end{pmatrix} \begin{pmatrix} 1 & 0 \\ -\hat{p}(\omega) & 1 \end{pmatrix}, \quad (21)$$

where $\hat{p}(\omega)$ is defined by $\sum_k p(c_j[k])e^{-i\omega k} = \hat{p}(\omega)\hat{c}_j(\omega)$, and similarly for the updater $\hat{u}(\omega)$. One can immediately recognize that these factorized matrices are all invertible, and hence it is easy to construct the dual polyphase matrix by taking its inverse $\hat{\tilde{P}}(\omega) = \hat{P}(\omega)^\dagger^{-1}$.

For example, the simple choice $\hat{p}(\omega) = 1$, $\hat{u}(\omega) = 1/2$, and $K = \sqrt{2}$ gives the orthogonal Haar filters $\hat{h}(\omega) = \hat{\tilde{h}}(\omega) = (1 + e^{-i\omega})/\sqrt{2}$ and $\hat{g}(\omega) = \hat{\tilde{g}}(\omega) = (-1 + e^{-i\omega})/\sqrt{2}$. The predictor operator uses the even component $c_j[2k]$ at its left neighboring odd component $c_j[2k+1]$. The order of the predictor is one [15]. The prediction is accurate if a signal is constant or, in other words, zeroth-order polynomial.

If we choose the linear prediction

$$\hat{p}(\omega) = \frac{1 + e^{-i\omega}}{2}, \quad \hat{u}(\omega) = \frac{1 + e^{i\omega}}{4}, \quad (22)$$

and $K = \sqrt{2}$, we obtain CDF(2, 2) biorthogonal filters [20]

$$\hat{h}(\omega) = \frac{-e^{i2\omega} + 2e^{i\omega} + 6 + 2e^{-i\omega} - e^{-i2\omega}}{4\sqrt{2}}, \quad (23)$$

$$\hat{g}(\omega) = \frac{-1 + 2e^{-i\omega} - e^{-i2\omega}}{2\sqrt{2}}.$$

In this linear case, the order of the predictor is two, which predicts first-order polynomials of a signal. Both HP filters $\hat{g}(\omega)$ and $\hat{\tilde{g}}(\omega)$ have second-order zeros at $\omega = 0$ while LP filters $\hat{h}(\omega)$ and $\hat{\tilde{h}}(\omega)$ have the same number of zeros at $\omega = \pi$. Correspondingly, the wavelets $(\psi, \tilde{\psi})$, shown together with $(\phi, \tilde{\phi})$ in Figure 1, have 2 vanishing moments, respectively. Different choices of \hat{p} and \hat{u} lead other types of CDF biorthogonal filters or any FIR filters used for the wavelet transforms [21]. We now introduce the method to design higher-order predictors based on a polynomial interpolation.

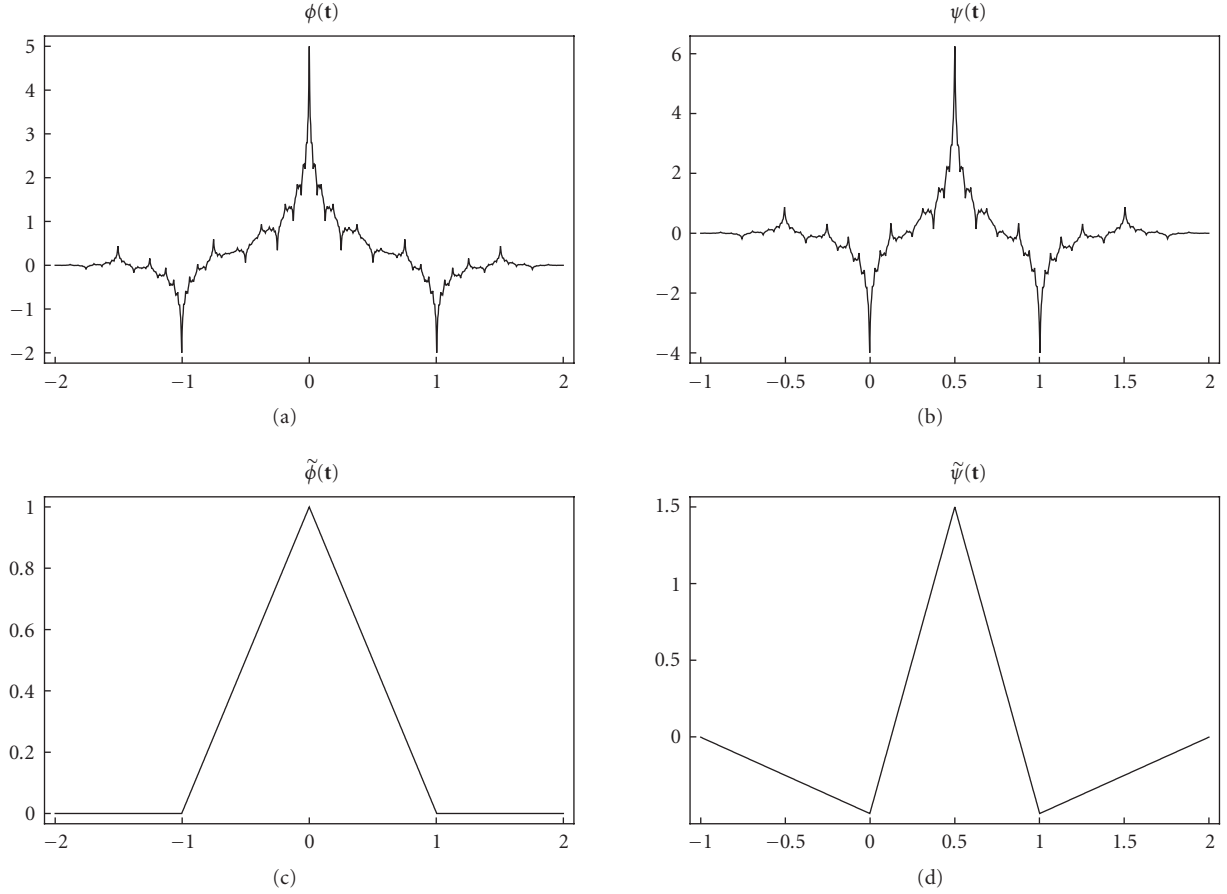


FIGURE 1: The system $(\phi, \psi, \tilde{\phi}, \tilde{\psi})$ of CDF(2, 2) biorthogonal wavelets with 2 vanishing moments.

2.3. Interpolating Wavelets. To build a higher-order predictor, we use the Lagrange interpolation scheme. The corresponding interpolating filter is Lagrange half-band filter [22], which is a symmetric maxflat filter that satisfies $\hat{h}(\omega) = \hat{h}(-\omega)$ and

$$\hat{h}(\omega) + \hat{h}(\omega + \pi) = \sqrt{2}. \quad (24)$$

The filter has $2L + 1$ nonzero coefficients and is the shortest filter that reproduces mid-values of polynomials of degree $2L - 1$ from a given set of samples. Therefore, the Lagrange half-band filter can directly be used as a $2L$ th-order predictor of the lifting scheme. For any $L \geq 1$ and $-L < k \leq L$, the coefficients are given in an explicit form as

$$h^L[2k - 1] = \frac{(-1)^{L+k-1} \prod_{n=1}^{2L} (L - n + 1/2)}{(L + k - 1)!(L - k)!(k - 1/2)}, \quad (25)$$

and the even coefficients are constrained as $h^L[2k] = \delta[k]$. They are also known to be identical to those of the Deslauriers-Dubuc filters [23, 24] of order $N = 2L$.

When the odd coefficients of the L th-order Lagrange half-band filter are chosen to be a predictor $p[k]$ of order N

$$p[k] = p^N[k] = h^L[2k - 1], \quad (26)$$

one can set an updater as

$$\hat{u}(\omega) = \frac{\hat{p}^{\tilde{N}*}(\omega)}{2} \quad \text{for } \tilde{N} \leq N. \quad (27)$$

As a result, we can obtain a family of (N, \tilde{N}) interpolating wavelet filters constructed in [8], where (N, \tilde{N}) denotes the number of vanishing moments of HP filters (g, \tilde{g}) . They are a set of symmetric biorthogonal perfect reconstruction FIR filters $(h, \tilde{h}, g, \tilde{g})$, where \tilde{h} is equivalent to the Lagrange half-band filter (25) of order $2L = N$, and the corresponding dual scaling function $\tilde{\phi}$ is an interpolating function that recovers polynomials of degree $N - 1$. It is remarkable to note that $\hat{h}(\omega)\hat{h}^*(\omega)$ in case $N = \tilde{N}$ gives rise to the orthogonal maxflat Daubechies filter with N vanishing moments [22].

The case $(N = 2, \tilde{N} = 2)$ amounts to CDF(2, 2) filters (23) whose wavelet and scaling functions are shown in Figure 1. The dual scaling function is a linear hat function. Since the lifting does not guarantee the stability of bases, these both primal functions are known to be not a stable basis, as we might recognize in their irregular shapes. However, this is only the case for $(N = 2, \tilde{N} = 2)$. The function is stable and its regularity increases when choosing the order more than two.

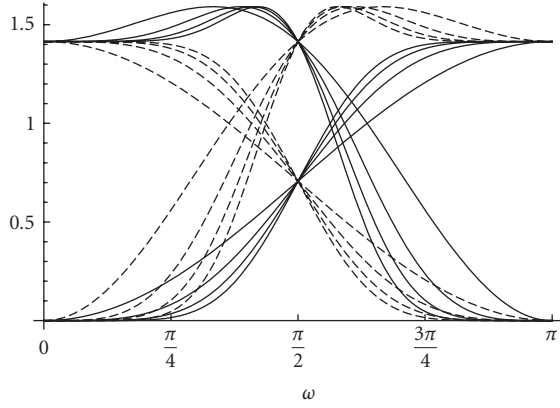


FIGURE 2: Frequency responses of (N, \tilde{N}) interpolating filters $(|\hat{h}(\omega)|, |\hat{h}(\omega)|, |\hat{g}(\omega)|, |\hat{g}(\omega)|)$ for even orders 2 to 8 in case $N = \tilde{N}$, which are obtained according to the coefficients given in Table 1. Solid line and dashed line represent primal and dual filters, respectively. As N and \tilde{N} increase, the filters are increasingly flat at $\omega = 0$ and $\omega = \pi$.

Table 1 shows the different orders of predictor $p^N[k]$ based on Lagrange half-band filters defined in (26). The frequency responses of corresponding filters $(h, \hat{h}, g, \tilde{g})$ are shown in Figure 2. As N and \tilde{N} increase, the filters are increasingly flat at $\omega = 0$ and $\omega = \pi$, which implies that a lack of smoothness of a signal after the decomposition would be improved. Their filter coefficients are always of the form $z/2^n$ where $z \in \mathbb{Z}$, $n \in \mathbb{N}$, thereby allowing an implementation of the integer wavelet transform [25], which has been adopted in the JPEG2000 standard.

3. Triangular Biorthogonal Wavelets

This section presents triangular wavelets, which are two-dimensional nonseparable wavelets defined on a regular triangular lattice. The construction basically follows a straightforward generalization of the interpolating wavelets described before. We first study a method for generating the triangular lattice. Then we show how the filters as well as wavelets constructed in Section 2 fit into the general settings.

3.1. Bravais Lattice Formalism. A discrete signal is naturally indexed by integers in one dimension, but the indexing may become a nontrivial problem in two or higher dimensions. Here we introduce a convenient method of site indexing for a two-dimensional plane by employing the primitive translation vectors. In solid state physics, possible crystals are classified as lattice structures called Bravais lattice generated by three primitive translation vectors. While general crystals have three-dimensional structures, the basic idea is still applicable in two dimension and poses no basic problems. We begin our formulation following the general strategy in solid state physics for example [26].

We define two primitive translation vectors

$$\mathbf{t}_1 = \begin{pmatrix} 1 & 0 \end{pmatrix}^T, \quad \mathbf{t}_2 = \begin{pmatrix} -\frac{1}{2} & \frac{\sqrt{3}}{2} \end{pmatrix}^T, \quad (28)$$

with which the regular triangular Bravais lattice is defined by

$$\Lambda = \{\mathbf{t} = n_1 \mathbf{t}_1 + n_2 \mathbf{t}_2 \mid (n_1, n_2) \in \mathbb{Z}^2\}. \quad (29)$$

The domain containing all the points whose closest site is a site $\mathbf{t} \in \Lambda$ is the Wigner-Seitz cell of the site, which is also called the Voronoi cell. It is the domain of definition of a function $f(\mathbf{r})$, $\mathbf{r} \in \mathbb{R}^2$. Each site belongs to its corresponding Wigner-Seitz cell, and a whole plane \mathbb{R}^2 is represented as a tiling of the cells. For a two-dimensional discrete signal such as an image, this plays the role of a pixel. In our setting the Wigner-Seitz cell is a hexagon, as shown in Figure 3.

The reciprocal lattice vectors are similarly defined by

$$\boldsymbol{\lambda}_1 = \begin{pmatrix} 0 & \frac{2}{\sqrt{3}} \end{pmatrix}^T, \quad \boldsymbol{\lambda}_2 = \begin{pmatrix} 1 & \frac{1}{\sqrt{3}} \end{pmatrix}^T, \quad (30)$$

which generate the reciprocal lattice

$$\hat{\Lambda} = \{2\pi(\boldsymbol{\lambda} = n_1 \boldsymbol{\lambda}_1 + n_2 \boldsymbol{\lambda}_2) \mid (n_1, n_2) \in \mathbb{Z}^2\}. \quad (31)$$

The Wigner-Seitz cell of the reciprocal lattice $\hat{\Lambda}$ is called the Brillouin zone, which is also a hexagon (see Figure 3). Analogous to the nature of the Wigner-Seitz cells, a whole $\boldsymbol{\omega}$ -plane can also be tiled by a set of Brillouin zones, as illustrated together in Figure 4.

For notational convenience we also define $\mathbf{t}_0 = \boldsymbol{\lambda}_0 = 0$, $\mathbf{t}_3 = -\mathbf{t}_1 - \mathbf{t}_2$, and $\boldsymbol{\lambda}_3 = \boldsymbol{\lambda}_1 - \boldsymbol{\lambda}_2$, holding the relation

$$\boldsymbol{\lambda}_m \cdot \mathbf{t}_m = 0, \quad m = 0, 1, 2, 3. \quad (32)$$

Note that \mathbf{t}_3 and $\boldsymbol{\lambda}_3$ are not linearly independent and in particular

$$e^{-i\pi n \boldsymbol{\lambda}_i \cdot \mathbf{t}_j} = \begin{cases} 1, & i = j, \\ (-1)^n, & i \neq j, \end{cases} \quad i, j = 1, 2, 3, \quad n \in \mathbb{Z}. \quad (33)$$

A discrete signal $\{c_j[\mathbf{t}]\}_{\mathbf{t} \in \Lambda}$ is assumed to be given on the Bravais lattice Λ , and its Fourier transform

$$\hat{c}_j(\boldsymbol{\omega}) = \sum_{\mathbf{t} \in \Lambda} c_j[\mathbf{t}] e^{-i\boldsymbol{\omega} \cdot \mathbf{t}}, \quad \boldsymbol{\omega} \in \mathbb{R}^2, \quad (34)$$

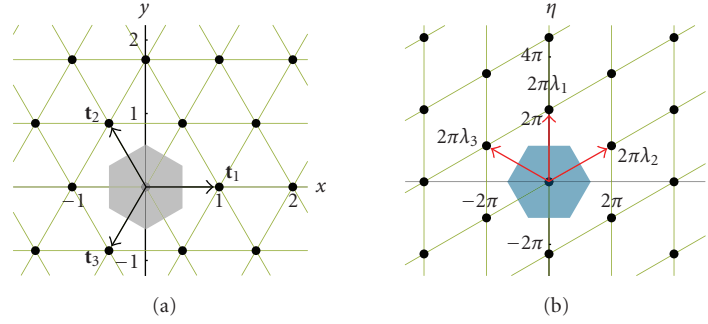
is doubly periodic with period $2\pi\boldsymbol{\lambda}$

$$\hat{c}_j(\boldsymbol{\omega}) = \hat{c}_j(\boldsymbol{\omega} + 2\pi\boldsymbol{\lambda}), \quad \boldsymbol{\lambda} \in \hat{\Lambda}. \quad (35)$$

Thus, one of the Brillouin zones is the domain of definition of $\hat{c}_j(\boldsymbol{\omega})$, which corresponds to the interval $[-\pi, \pi]$ in one dimension. In particular, the aliasing frequencies occur at the boundary of the Brillouin zones. Unlike the one-dimensional setting, where there exists only one alias point at $\omega = \pi$, we have three alias points at $\boldsymbol{\omega} = \pi\boldsymbol{\lambda}_k$, $k = 1, 2, 3$ due to the double periodicity.

TABLE 1: Coefficients for predictor $p^N[k]$ of order N based on Lagrange interpolation.

$N \setminus k$	-4	-3	-2	-1	0	1	2	3	4	5	Scaling
2					1	1					$/2$
4				-1	9	9	-1				$/2^4$
6			3	-25	150	150	-25	3			$/2^8$
8		-5	49	-245	1225	1225	-245	49	-5		$/2^{11}$
10	35	-405	567	-2205	19845	19845	-2205	567	-405	35	$/2^{16}$

FIGURE 3: Bravais lattice Λ generated by two primitive translation vectors \mathbf{t}_1 and \mathbf{t}_2 , and Wigner-Seitz cell (a); reciprocal lattice $\hat{\Lambda}$ generated by two reciprocal lattice vectors λ_1 and λ_2 , and Brillouin zone (b). For notational convenience \mathbf{t}_3 and λ_3 are also defined.

A crucial observation is that the Bravais lattice Λ may be split into four sublattices

$$\Lambda_m = \{2\mathbf{t} + \mathbf{t}_m \mid \mathbf{t} \in \Lambda\}, \quad m = 0, 1, 2, 3. \quad (36)$$

The set Λ is now partitioned, and these four sets Λ_m are completely disjoint from each other. If we add all of the sites of sublattices, then we recover the original lattice. This is exactly the polyphase decomposition of the Bravais lattice, which immediately indicates that we have four polyphase components and thus four patterns of indices (see Figure 5). For example, a signal $\{c_j[\mathbf{t}]\}_{\mathbf{t} \in \Lambda}$ is represented as its four polyphase components

$$\hat{c}_{m,j}(\boldsymbol{\omega}) = \sum_{\mathbf{t} \in \Lambda} c_j[2\mathbf{t} + \mathbf{t}_m] e^{-i\boldsymbol{\omega} \cdot \mathbf{t}}, \quad m = 0, 1, 2, 3, \quad (37)$$

which play the role of even and odd indices in one dimension. Then the formula analogous to (11) is

$$\begin{pmatrix} \hat{c}_j(\boldsymbol{\omega}) \\ \hat{c}_j(\boldsymbol{\omega} + \pi\lambda_1) \\ \hat{c}_j(\boldsymbol{\omega} + \pi\lambda_2) \\ \hat{c}_j(\boldsymbol{\omega} + \pi\lambda_3) \end{pmatrix} = \hat{U}(\boldsymbol{\omega}) \begin{pmatrix} \hat{c}_{0,j}(2\boldsymbol{\omega}) \\ \hat{c}_{1,j}(2\boldsymbol{\omega}) \\ \hat{c}_{2,j}(2\boldsymbol{\omega}) \\ \hat{c}_{3,j}(2\boldsymbol{\omega}) \end{pmatrix}, \quad (38)$$

where

$$\hat{U}(\boldsymbol{\omega}) = \begin{pmatrix} 1 & e^{-i\boldsymbol{\omega} \cdot \mathbf{t}_1} & e^{-i\boldsymbol{\omega} \cdot \mathbf{t}_2} & e^{-i\boldsymbol{\omega} \cdot \mathbf{t}_3} \\ 1 & e^{-i\boldsymbol{\omega} \cdot \mathbf{t}_1} & -e^{-i\boldsymbol{\omega} \cdot \mathbf{t}_2} & -e^{-i\boldsymbol{\omega} \cdot \mathbf{t}_3} \\ 1 & -e^{-i\boldsymbol{\omega} \cdot \mathbf{t}_1} & e^{-i\boldsymbol{\omega} \cdot \mathbf{t}_2} & -e^{-i\boldsymbol{\omega} \cdot \mathbf{t}_3} \\ 1 & -e^{-i\boldsymbol{\omega} \cdot \mathbf{t}_1} & -e^{-i\boldsymbol{\omega} \cdot \mathbf{t}_2} & e^{-i\boldsymbol{\omega} \cdot \mathbf{t}_3} \end{pmatrix}. \quad (39)$$

In order to obtain the wavelet transform applied to our triangular lattice, the filters used for the decomposition

and reconstruction must be formed by a set of four filters, because we have four polyphase components. The straightforward generalization shows that the possible combination of four filters turns out to be one LP and three independent HP filters $\{h[\mathbf{t}], g_1[\mathbf{t}], g_2[\mathbf{t}], g_3[\mathbf{t}]\}_{\mathbf{t} \in \Lambda}$, which satisfies

$$\begin{aligned} \hat{h}(\boldsymbol{\omega})\hat{h}^*(\boldsymbol{\omega}) + \sum_{m=1}^3 \hat{g}_m(\boldsymbol{\omega})\hat{g}_m^*(\boldsymbol{\omega}) &= 4, \\ \hat{h}(\boldsymbol{\omega})\hat{h}^*(\boldsymbol{\omega} + \pi\lambda_1) + \sum_{m=1}^3 \hat{g}_m(\boldsymbol{\omega})\hat{g}_m^*(\boldsymbol{\omega} + \pi\lambda_1) &= 0, \\ \hat{h}(\boldsymbol{\omega})\hat{h}^*(\boldsymbol{\omega} + \pi\lambda_2) + \sum_{m=1}^3 \hat{g}_m(\boldsymbol{\omega})\hat{g}_m^*(\boldsymbol{\omega} + \pi\lambda_2) &= 0, \\ \hat{h}(\boldsymbol{\omega})\hat{h}^*(\boldsymbol{\omega} + \pi\lambda_3) + \sum_{m=1}^3 \hat{g}_m(\boldsymbol{\omega})\hat{g}_m^*(\boldsymbol{\omega} + \pi\lambda_3) &= 0, \end{aligned} \quad (40)$$

or in terms of the modulation matrix

$$\hat{M}^T(\boldsymbol{\omega})\hat{M}^*(\boldsymbol{\omega}) = 4I, \quad (41)$$

where

$$\hat{M}(\boldsymbol{\omega}) = \begin{pmatrix} \hat{h}(\boldsymbol{\omega}) & \hat{h}(\boldsymbol{\omega} + \pi\lambda_1) & \hat{h}(\boldsymbol{\omega} + \pi\lambda_2) & \hat{h}(\boldsymbol{\omega} + \pi\lambda_3) \\ \hat{g}_1(\boldsymbol{\omega}) & \hat{g}_1(\boldsymbol{\omega} + \pi\lambda_1) & \hat{g}_1(\boldsymbol{\omega} + \pi\lambda_2) & \hat{g}_1(\boldsymbol{\omega} + \pi\lambda_3) \\ \hat{g}_2(\boldsymbol{\omega}) & \hat{g}_2(\boldsymbol{\omega} + \pi\lambda_1) & \hat{g}_2(\boldsymbol{\omega} + \pi\lambda_2) & \hat{g}_2(\boldsymbol{\omega} + \pi\lambda_3) \\ \hat{g}_3(\boldsymbol{\omega}) & \hat{g}_3(\boldsymbol{\omega} + \pi\lambda_1) & \hat{g}_3(\boldsymbol{\omega} + \pi\lambda_2) & \hat{g}_3(\boldsymbol{\omega} + \pi\lambda_3) \end{pmatrix}, \quad (42)$$

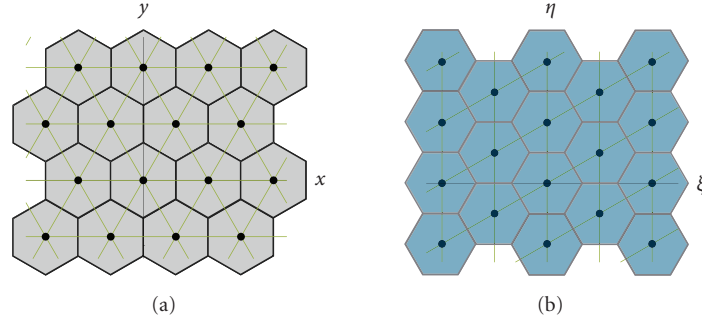


FIGURE 4: Set of Wigner-Seitz cells (a) and Brillouin zones (b) in Bravais lattice Λ and reciprocal lattice $\hat{\Lambda}$, respectively. Both whole plane \mathbb{R}^2 can be represented as a tiling of them.

and $\hat{M}(\omega)$ is defined in a similar way. As in one dimension, the set of these four filters produces a scaling function ϕ and wavelets ψ_m , $m = 1, 2, 3$ defined on \mathbb{R}^2

$$\hat{\phi}(\omega) = \frac{1}{2} \hat{h}\left(\frac{\omega}{2}\right) \hat{\phi}\left(\frac{\omega}{2}\right), \quad \hat{\psi}_m(\omega) = \frac{1}{2} \hat{g}_m\left(\frac{\omega}{2}\right) \hat{\phi}\left(\frac{\omega}{2}\right), \quad (43)$$

which are normalized as $\hat{\phi}(0) = 1$ and $\hat{\psi}_m(0) = 0$, assuming that $\hat{h}[0] = 2$ and $\hat{g}[0] = 0$. Note that we have three wavelets. On the Bravais lattice Λ they satisfy the relation

$$\begin{aligned} \phi(\mathbf{r}) &= \sum_{\mathbf{t} \in \Lambda} 2h[\mathbf{t}] \phi(2\mathbf{r} - \mathbf{t}), \\ \psi_m(\mathbf{r}) &= \sum_{\mathbf{t} \in \Lambda} 2g_m[\mathbf{t}] \phi(2\mathbf{r} - \mathbf{t}). \end{aligned} \quad (44)$$

The dual scaling function and wavelets are formed similarly.

3.2. Triangular Wavelet Transform. Corresponding to the decomposition of the Bravais lattice Λ , the polyphase representation of a LP filter $\{h[\mathbf{t}]\}_{\mathbf{t} \in \Lambda}$ and three HP filters $\{g_k[\mathbf{t}]\}_{\mathbf{t} \in \Lambda}$, $k = 1, 2, 3$, are given by the following form:

$$\begin{aligned} & \left(\hat{h}(\omega) \quad \hat{g}_1(\omega) \quad \hat{g}_2(\omega) \quad \hat{g}_3(\omega) \right)^T \\ &= \begin{pmatrix} \hat{h}_0(2\omega) & \hat{h}_1(2\omega) & \hat{h}_2(2\omega) & \hat{h}_3(2\omega) \\ \hat{g}_{1,0}(2\omega) & \hat{g}_{1,1}(2\omega) & \hat{g}_{1,2}(2\omega) & \hat{g}_{1,3}(2\omega) \\ \hat{g}_{2,0}(2\omega) & \hat{g}_{2,1}(2\omega) & \hat{g}_{2,2}(2\omega) & \hat{g}_{2,3}(2\omega) \\ \hat{g}_{3,0}(2\omega) & \hat{g}_{3,1}(2\omega) & \hat{g}_{3,2}(2\omega) & \hat{g}_{3,3}(2\omega) \end{pmatrix} \begin{pmatrix} 1 \\ e^{-i\omega \cdot \mathbf{t}_1} \\ e^{-i\omega \cdot \mathbf{t}_2} \\ e^{-i\omega \cdot \mathbf{t}_3} \end{pmatrix}, \end{aligned} \quad (45)$$

where

$$\begin{aligned} \hat{h}_m(\omega) &= \sum_{\mathbf{t} \in \Lambda} h[2\mathbf{t} + \mathbf{t}_m] e^{-i\omega \cdot \mathbf{t}}, \\ \hat{g}_{k,m}(\omega) &= \sum_{\mathbf{t} \in \Lambda} g_k[2\mathbf{t} + \mathbf{t}_m] e^{-i\omega \cdot \mathbf{t}}, \end{aligned} \quad m = 0, 1, 2, 3. \quad (46)$$

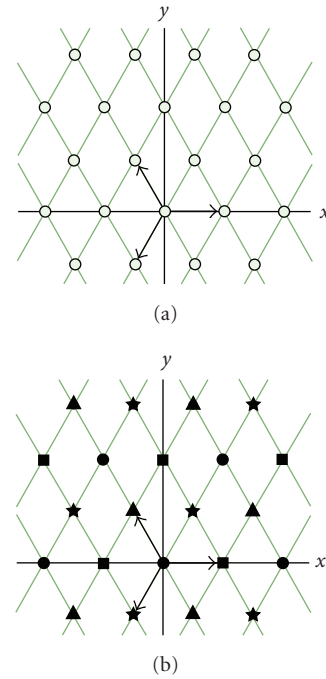


FIGURE 5: Polyphase decomposition of the Bravais lattice Λ (a) into four sublattices Λ_m , $m = 0, 1, 2, 3$ (b). Circle mark (a) represents original lattice sites while under side of circle, square, triangle, and star marks (b) represents each polyphase of four sublattices according to directions in \mathbf{t}_0 , \mathbf{t}_1 , \mathbf{t}_2 , and \mathbf{t}_3 , respectively.

We then assemble the polyphase matrix as

$$\hat{P}(\omega) = \begin{pmatrix} \hat{h}_0(\omega) & \hat{g}_{1,0}(\omega) & \hat{g}_{2,0}(\omega) & \hat{g}_{3,0}(\omega) \\ \hat{h}_1(\omega) & \hat{g}_{1,1}(\omega) & \hat{g}_{2,1}(\omega) & \hat{g}_{3,1}(\omega) \\ \hat{h}_2(\omega) & \hat{g}_{1,2}(\omega) & \hat{g}_{2,2}(\omega) & \hat{g}_{3,2}(\omega) \\ \hat{h}_3(\omega) & \hat{g}_{1,3}(\omega) & \hat{g}_{2,3}(\omega) & \hat{g}_{3,3}(\omega) \end{pmatrix}, \quad (47)$$

and dual polyphase matrix $\hat{P}(\omega)$ similarly.

Now we are ready to define the triangular wavelet transform. With a particular set of four filters, a signal \hat{c}_j is

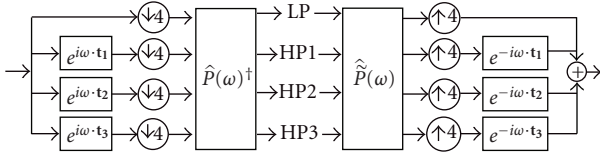


FIGURE 6: Poplyphase representation of triangular wavelet transform. First signal is decomposed into four phases subsampled by 4, then they are filtered by applying the polyphase matrix to yield the coarse (LP) and three detail (HP) components. The inverse transform is simply realized with the dual polyphase matrix by taking the exactly backward procedure.

decomposed into a coarse component \hat{c}_{j-1} and three detail components $\hat{d}_{m,j-1}$, $m = 1, 2, 3$, subsampled by a factor of 4

$$\begin{pmatrix} \hat{c}_{j-1}(\boldsymbol{\omega}) \\ \hat{d}_{1,j-1}(\boldsymbol{\omega}) \\ \hat{d}_{2,j-1}(\boldsymbol{\omega}) \\ \hat{d}_{3,j-1}(\boldsymbol{\omega}) \end{pmatrix} = \hat{P}(\boldsymbol{\omega})^\dagger \begin{pmatrix} \hat{c}_{0,j}(\boldsymbol{\omega}) \\ \hat{c}_{1,j}(\boldsymbol{\omega}) \\ \hat{c}_{2,j}(\boldsymbol{\omega}) \\ \hat{c}_{3,j}(\boldsymbol{\omega}) \end{pmatrix}, \quad (48)$$

which is illustrated schematically in Figure 6. The original signal \hat{c}_j can be reconstructed by the inverse transform

$$\begin{pmatrix} \hat{c}_{0,j}(\boldsymbol{\omega}) \\ \hat{c}_{1,j}(\boldsymbol{\omega}) \\ \hat{c}_{2,j}(\boldsymbol{\omega}) \\ \hat{c}_{3,j}(\boldsymbol{\omega}) \end{pmatrix} = \hat{P}(\boldsymbol{\omega}) \begin{pmatrix} \hat{c}_{j-1}(\boldsymbol{\omega}) \\ \hat{d}_{1,j-1}(\boldsymbol{\omega}) \\ \hat{d}_{2,j-1}(\boldsymbol{\omega}) \\ \hat{d}_{3,j-1}(\boldsymbol{\omega}) \end{pmatrix}, \quad (49)$$

assuming that the perfect reconstruction condition is satisfied

$$\hat{P}(\boldsymbol{\omega})\hat{P}(\boldsymbol{\omega})^\dagger = I. \quad (50)$$

As we see in Figure 6, the structure of the triangular wavelet transform is essentially the same as that of a four-channel filter bank for a two-dimensional signal. On the lattice plane the decomposition and the reconstruction are defined by convolutions and subsampling of the output by 4. This can be written in terms of the extension of the Mallat algorithm [27]

$$\begin{aligned} \hat{c}_{j-1}[\mathbf{t}] &= \sum_{\mathbf{s} \in \Lambda} h^*[\mathbf{s} - 2\mathbf{t}]c_j[\mathbf{s}], \\ \hat{d}_{m,j-1}[\mathbf{t}] &= \sum_{\mathbf{s} \in \Lambda} g_m^*[\mathbf{s} - 2\mathbf{t}]c_j[\mathbf{s}], \\ c_j[\mathbf{t}] &= \sum_{\mathbf{s} \in \Lambda} \left(\tilde{h}[\mathbf{t} - 2\mathbf{s}]c_{j-1}[\mathbf{s}] + \sum_{m=1}^3 \tilde{g}_m[\mathbf{t} - 2\mathbf{s}]d_{m,j-1}[\mathbf{s}] \right). \end{aligned} \quad (51)$$

Recall that the lifting scheme corresponds to the factorization of a polyphase matrix. It allows one to construct any biorthogonal filters as well as fast in-place implementation

of the wavelet transform that require less computational cost than the direct implementations (51). We now wish to extend the factorization (21) to our case, which is found to be

$$\begin{aligned} \hat{P}(\boldsymbol{\omega})^\dagger &= \begin{pmatrix} K & 0 & 0 & 0 \\ 0 & \frac{1}{K} & 0 & 0 \\ 0 & 0 & \frac{1}{K} & 0 \\ 0 & 0 & 0 & \frac{1}{K} \end{pmatrix} \\ &\times \begin{pmatrix} 1 & \hat{u}_1(\boldsymbol{\omega}) & \hat{u}_2(\boldsymbol{\omega}) & \hat{u}_3(\boldsymbol{\omega}) \\ 0 & 1 & 0 & 0 \\ 0 & 0 & 1 & 0 \\ 0 & 0 & 0 & 1 \end{pmatrix} \begin{pmatrix} 1 & 0 & 0 & 0 \\ -\hat{p}_1(\boldsymbol{\omega}) & 1 & 0 & 0 \\ -\hat{p}_2(\boldsymbol{\omega}) & 0 & 1 & 0 \\ -\hat{p}_3(\boldsymbol{\omega}) & 0 & 0 & 1 \end{pmatrix}, \end{aligned} \quad (52)$$

with three predictors \hat{p}_m and updaters \hat{u}_m , $m = 1, 2, 3$. Obviously, these matrices are still invertible. The lifting implementation of the triangular wavelet transform is then realized by the following steps. First, we have three predict steps; three odd components $c_j[2\mathbf{t} + \mathbf{t}_m]$, $m = 1, 2, 3$, are predicted by three predictors p_m , respectively,

$$\begin{aligned} c_j[2\mathbf{t} + \mathbf{t}_1] &\rightarrow d_{1,j-1}[\mathbf{t}] = c_j[2\mathbf{t} + \mathbf{t}_1] - p_1(c_j[2\mathbf{t}]), \\ c_j[2\mathbf{t} + \mathbf{t}_2] &\rightarrow d_{2,j-1}[\mathbf{t}] = c_j[2\mathbf{t} + \mathbf{t}_2] - p_2(c_j[2\mathbf{t}]), \\ c_j[2\mathbf{t} + \mathbf{t}_3] &\rightarrow d_{3,j-1}[\mathbf{t}] = c_j[2\mathbf{t} + \mathbf{t}_3] - p_3(c_j[2\mathbf{t}]). \end{aligned} \quad (53)$$

Then the update step is carried out dealing with three results of the prediction

$$c_j[2\mathbf{t}] \rightarrow c_{j-1}[\mathbf{t}] = c_j[2\mathbf{t}] + \sum_{m=1}^3 u_m(d_{m,j-1}[\mathbf{t}]), \quad (54)$$

which preserves the average of a two-dimensional signal. Finally the normalization steps are applied.

Since we take three predict steps, we have degrees of freedom to design three independent HP filters. If we make the filters isotropic, the energy of three detail components $d_{m,j-1}$ is expected to be evenly distributed while the diagonal detail component in the tensor product transform is not essentially the independent component. The factorization (52) for M -channel case is also considered in [28], where the individual predictors are modified depending on the situations. In our setting, we directly use the one-dimensional predictor for each predictor p_m in (52), and its subscript m corresponds to the directions of symmetric primitive translation vectors \mathbf{t}_m . This gives much easier extension of one-dimensional filters and obtains three isotropic HP filters whose coefficients on the triangular lattice are symmetrically arranged with respect to the origin. Moreover, this trigonal arrangement of filter coefficients provides hexagonal symmetry for the LP filter if each updater u_m is also set in a similar manner. We now proceed to construct such filters and discuss their properties.

3.3. *Triangular Interpolating Wavelets.* In this section we extend (N, \tilde{N}) interpolating filters presented in Section 2.2 including the Haar filter to the triangular lattice using (52). As in one dimension, the simplest choice

$$K = 2, \quad \hat{p}_m(\omega) = 1, \quad \hat{u}_m(\omega) = \frac{1}{4}, \quad m = 1, 2, 3, \quad (55)$$

and $\hat{P}(\omega) = \hat{P}(\omega)^{\dagger-1}$ gives two-dimensional Haar filters defined on the lattice, which turn out to be biorthogonal

$$\begin{pmatrix} \hat{h}(\omega) \\ \hat{g}_1(\omega) \\ \hat{g}_2(\omega) \\ \hat{g}_3(\omega) \end{pmatrix} = \frac{1}{2} \begin{pmatrix} 1 & 1 & 1 & 1 \\ -1 & 1 & 0 & 0 \\ -1 & 0 & 1 & 0 \\ -1 & 0 & 0 & 1 \end{pmatrix} \begin{pmatrix} 1 \\ e^{-i\omega \cdot \mathbf{t}_1} \\ e^{-i\omega \cdot \mathbf{t}_2} \\ e^{-i\omega \cdot \mathbf{t}_3} \end{pmatrix}, \quad (56)$$

$$\begin{pmatrix} \hat{h}(\omega) \\ \hat{g}_1(\omega) \\ \hat{g}_2(\omega) \\ \hat{g}_3(\omega) \end{pmatrix} = \frac{1}{2} \begin{pmatrix} 1 & 1 & 1 & 1 \\ -1 & 3 & -1 & -1 \\ -1 & -1 & 3 & -1 \\ -1 & -1 & -1 & 3 \end{pmatrix} \begin{pmatrix} 1 \\ e^{-i\omega \cdot \mathbf{t}_1} \\ e^{-i\omega \cdot \mathbf{t}_2} \\ e^{-i\omega \cdot \mathbf{t}_3} \end{pmatrix}.$$

In a similar way, we generalize (N, \tilde{N}) interpolating filters by letting predictors p_m as $p_m^N[k\mathbf{t}_m] = p^N[k]$, where $p^N[k]$ is given in Table 1 and slightly rewriting condition (27) as

$$\hat{u}_m(\omega) = \frac{\hat{P}_m^{\tilde{N}*}(\omega)}{4} \quad \text{for } \tilde{N} \leq N. \quad (57)$$

A set of resulting filters $(h, \tilde{h}, g_m, \tilde{g}_m)$ is (N, \tilde{N}) interpolating filters defined on the triangular lattice. Since our construction is straightforward generalization of the one-dimensional case, the dual LP filter \tilde{h} is still interpolating or half-band in the sense that

$$\hat{h}(\omega) + \sum_{m=1}^3 \hat{h}(\omega + \pi\lambda_m) = 2, \quad (58)$$

which is in place of (24). If we extend the linear prediction (22) according to (57)

$$\hat{p}_m(\omega) = \frac{1 + e^{-i\omega \cdot \mathbf{t}_m}}{2}, \quad \hat{u}_m(\omega) = \frac{1 + e^{i\omega \cdot \mathbf{t}_m}}{8}, \quad (59)$$

with $K = 2$, then we obtain the triangular version of $(2, 2)$ interpolating filters or CDF $(2, 2)$ filters. This shows that our method is general so that (N, \tilde{N}) interpolating filters of higher-order can be generalized directly.

For the Haar and $(2, 2)$ interpolating cases, we display the filter coefficients and their frequency responses with vectors $2\pi\lambda_m$ in Figures 7 and 8. In each case of $m = 1, 2, 3$, the coefficients of primal HP filters g_m are one dimensionally arranged along the directions of the primitive translation vectors \mathbf{t}_m . This is true for dual filters \tilde{g}_m while they have two-dimensional support on the lattice plane. In other words, this means that both HP filters (g_m, \tilde{g}_m) are isotropic as we exactly intended, and $m = 1$ and $m = 3$ cases are thus simply $2\pi/3$

TABLE 2: Number of zeros for triangular (N, \tilde{N}) interpolating filters.

	\hat{h}	\hat{g}_1	\hat{g}_2	\hat{g}_3	\hat{h}	\hat{g}_1	\hat{g}_2	\hat{g}_3
$\omega = \pi\lambda_1$	\tilde{N}	0	N	N	N	N	\tilde{N}	\tilde{N}
$\omega = \pi\lambda_2$	\tilde{N}	N	0	N	N	\tilde{N}	N	\tilde{N}
$\omega = \pi\lambda_3$	\tilde{N}	N	N	0	N	\tilde{N}	\tilde{N}	N

rotations of the $m = 2$ case. As we mentioned before, it is obvious that the triangular filters are periodic with respect to the translation $\omega \rightarrow \omega + 2\pi\lambda$, and (h, \tilde{h}) are intrinsically two-dimensional LP filters having the hexagonal symmetry.

Let us now concentrate on the nature of the triangular filters along the directions of reciprocal lattice vectors λ_m , $m = 1, 2, 3$. Due to the hexagonal symmetry, LP filters have the same structure for each direction of λ_m . In particular, we derive from (58) that they are also half-band

$$\hat{h}(\omega\lambda_k) + \hat{h}(\omega\lambda_m + \pi\lambda_m) = 2, \quad k, m = 1, 2, 3, \quad (60)$$

and the biorthogonality condition implies

$$\hat{h}^*(\omega\lambda_k)\hat{h}(\omega\lambda_k) + \hat{h}^*(\omega\lambda_m + \pi\lambda_m)\hat{h}(\omega\lambda_m + \pi\lambda_m) = 4. \quad (61)$$

Correspondingly, one-dimensional responses of three HP filters for directions in λ_m are defined from the LP filters in a manner similar to (7). The relations are summarized as follows:

$$\hat{g}_k(\omega\lambda_m) = \begin{cases} 0, & k = m, \\ \frac{1}{2}e^{-i\omega\mathbf{t}_k \cdot \lambda_m}\hat{h}(\omega\lambda_m + \pi\lambda_m), & k \neq m, \end{cases} \quad (62)$$

$$\tilde{g}_k(\omega\lambda_m) = \begin{cases} \hat{h}(\omega\lambda_m + \pi\lambda_m), & k = m, \\ e^{-i\omega\mathbf{t}_k \cdot \lambda_m}\hat{h}(\omega\lambda_m + \pi\lambda_m), & k \neq m, \end{cases}$$

where exponential factors give ± 1 according to (33). In fact, the frequency responses of LP filters $\hat{h}(\omega\lambda_m)$ and $\hat{h}(\omega\lambda_m)$ amount to the one-dimensional cases shown in Figure 2, and hence the same holds for HP filters $\hat{g}_k(\omega\lambda_m)$ and $\tilde{g}_k(\omega\lambda_m)$ in case $k \neq m$. Note the different normalization factor.

The HP filters $(\hat{g}_m(\omega), \tilde{g}_m(\omega))$, $m = 1, 2, 3$, have (N, \tilde{N}) vanishing moments. More precisely, the vanishing moment that we consider here is the number of zeros of $\hat{g}_m(\omega\lambda_m)$ and $\tilde{g}_m(\omega\lambda_m)$ at $\omega = 0$. Similarly LP filters $\hat{h}(\omega\lambda_m)$ and $\tilde{h}(\omega\lambda_m)$ have zeros at $\omega = \pi$, which corresponds to the alias points $\omega = \pi\lambda_m$. The number of zeros of triangular (N, \tilde{N}) interpolating filters is summarized in Table 2.

Although the wavelet and scaling functions are often less important than the associated filters in applications, we mention some of their interesting properties. In one dimension the Haar scaling function $\phi(t)$, whose value is 1 over the interval $t \in [0, 1)$ and 0 otherwise is the most trivial case for filling the real line \mathbb{R} . However, this becomes much more complicated for the two-dimensional case as shown in Figure 9. Note that the primal and dual scaling

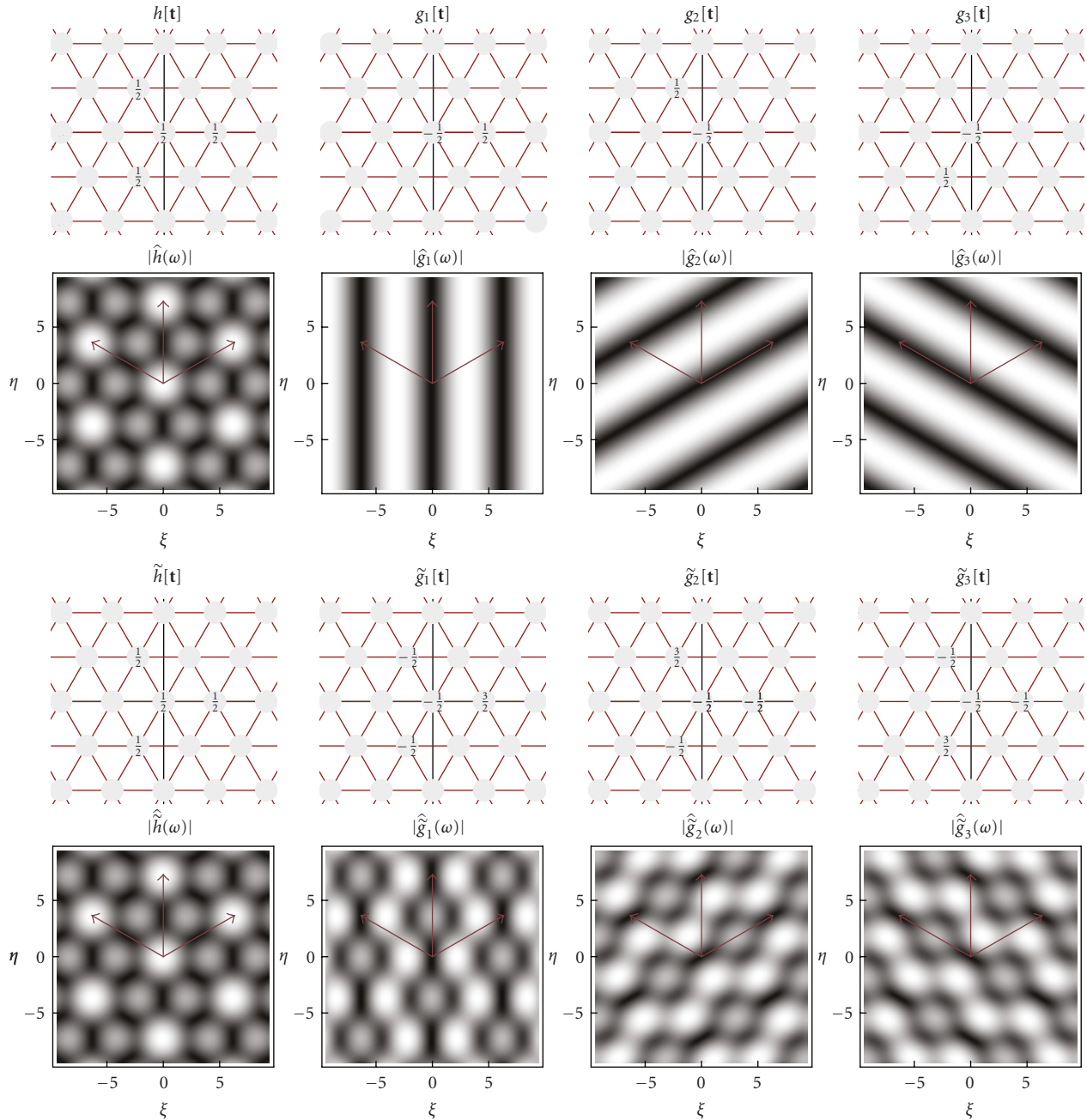


FIGURE 7: Frequency responses of triangular biorthogonal Haar filters ($h, g_m, \tilde{h}, \tilde{g}_m$), $m = 1, 2, 3$, whose arrows indicate 2π times reciprocal lattice vectors λ_m .

functions are identical and its value is 1 over the white region and 0 otherwise, while the wavelets have positive, zero, and negative values represented, respectively, in black, grey, and white. It is interesting to note that the scaling function with this fractal shape tiles a whole plane \mathbb{R}^2 . Such functions are also obtained in [29] on the rectangular setting $\mathbf{t}_1 = (1, 0)^T$ and $\mathbf{t}_2 = (0, 1)^T$ as one of the particular functions that have the property of self-similar tiling of \mathbb{R}^n . On the other hand, the set of $(2, 2)$ interpolating wavelets, shown also in Figure 9, is obviously no longer involved with a fractal shape. Their supports are based on the corresponding filters as given

in Figure 8 where LP filters h and \tilde{h} have the hexagonal symmetry. They are much more smooth functions but both primal functions still seem to contain jaggy parts, as we have already seen in their one-dimensional shapes shown in Figure 1. As we pointed out in Section 2, this lack of regularity is improved by increasing the order of N and \tilde{N} .

4. Applications

The main purpose in this section is to explore effective applications that are well suited for the triangular wavelets.

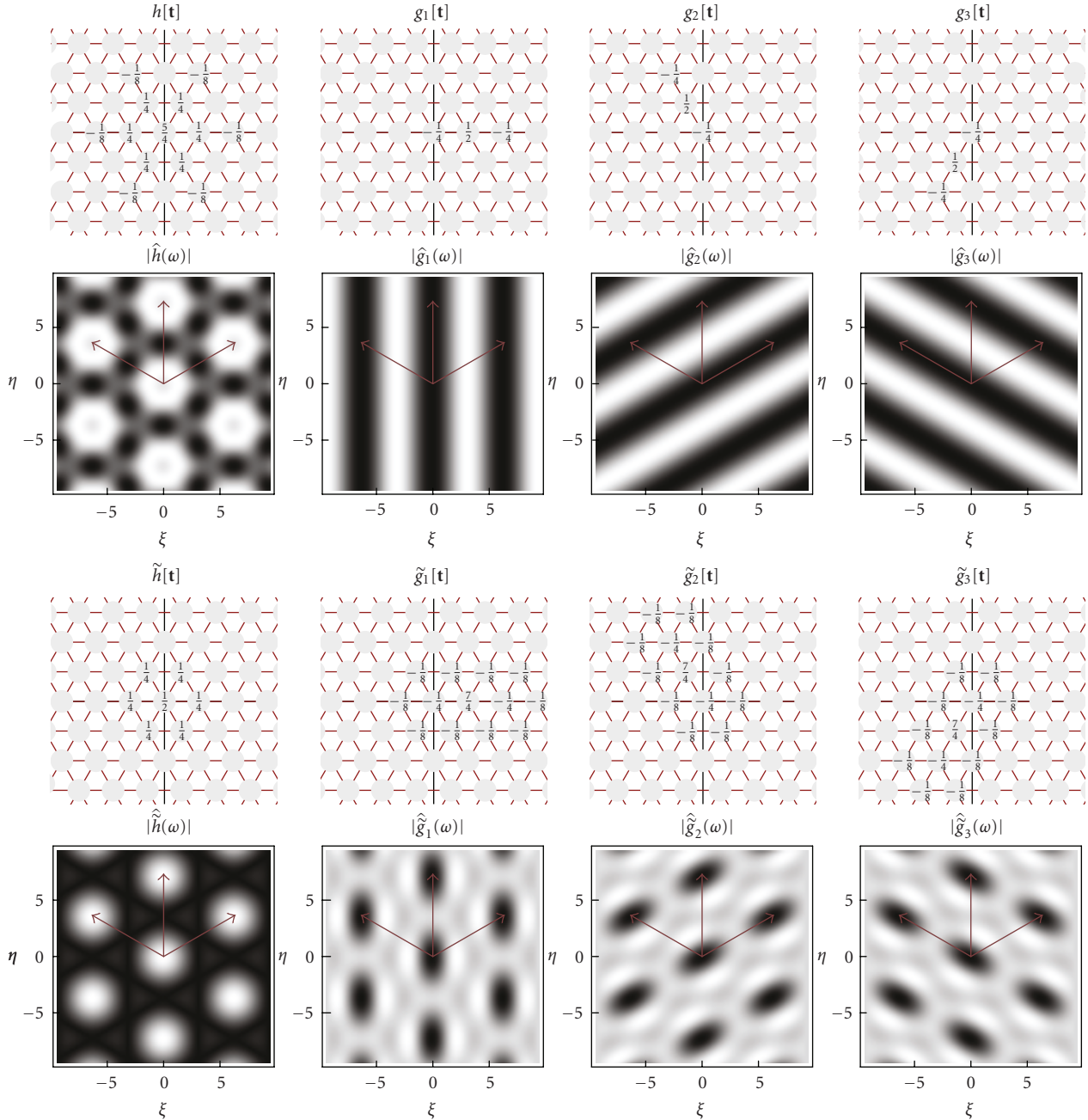


FIGURE 8: Frequency responses of triangular (N, \tilde{N}) interpolating filters $(h, g_m, \tilde{h}, \tilde{g}_m)$, $m = 1, 2, 3$, in case $N = \tilde{N} = 2$, whose arrows indicate 2π times reciprocal lattice vectors λ_m .

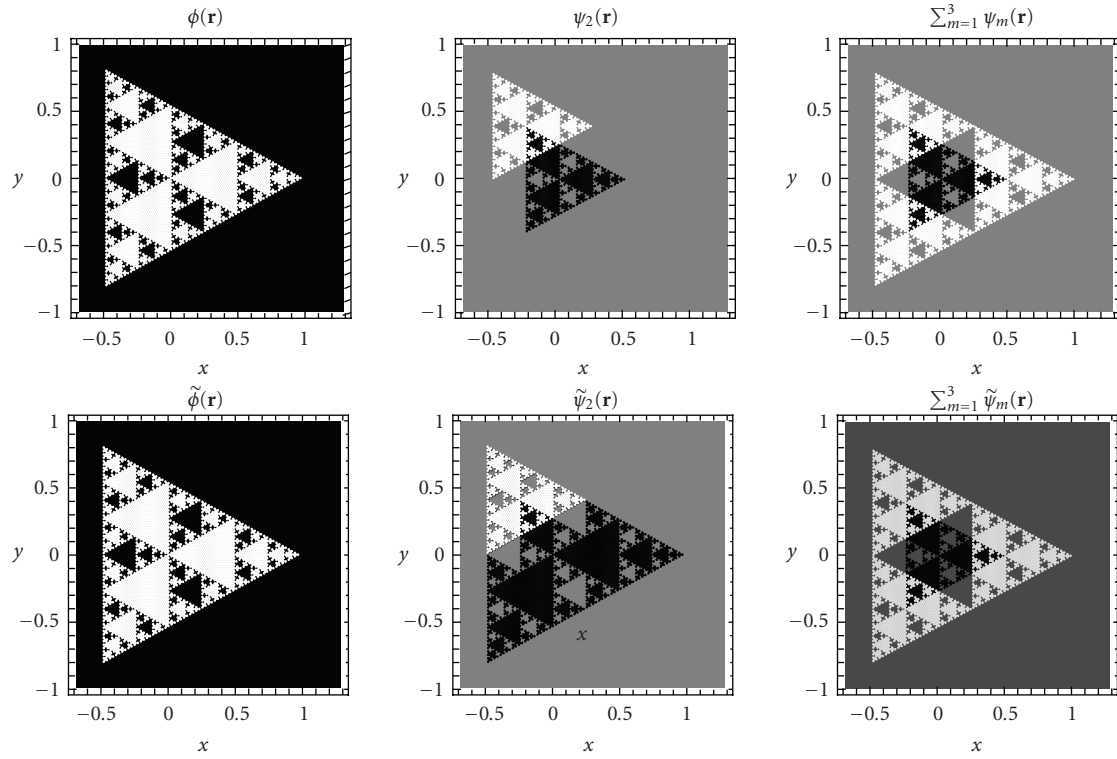
Triangular filters are applied to various images and their performances are compared with those in the conventional tensor product transform in terms of isotropy of images and quality of reconstruction.

4.1. Preliminaries. In the application of the triangular filters to images, the original data should represent hexagonal pixels arranged in a honeycomb structure. In the study of numerical computations, such data may easily be generated by sampling at Bravais lattice sites. Unfortunately, however, such data are not available in the standard image database, and hence we employ the following convention. We assume

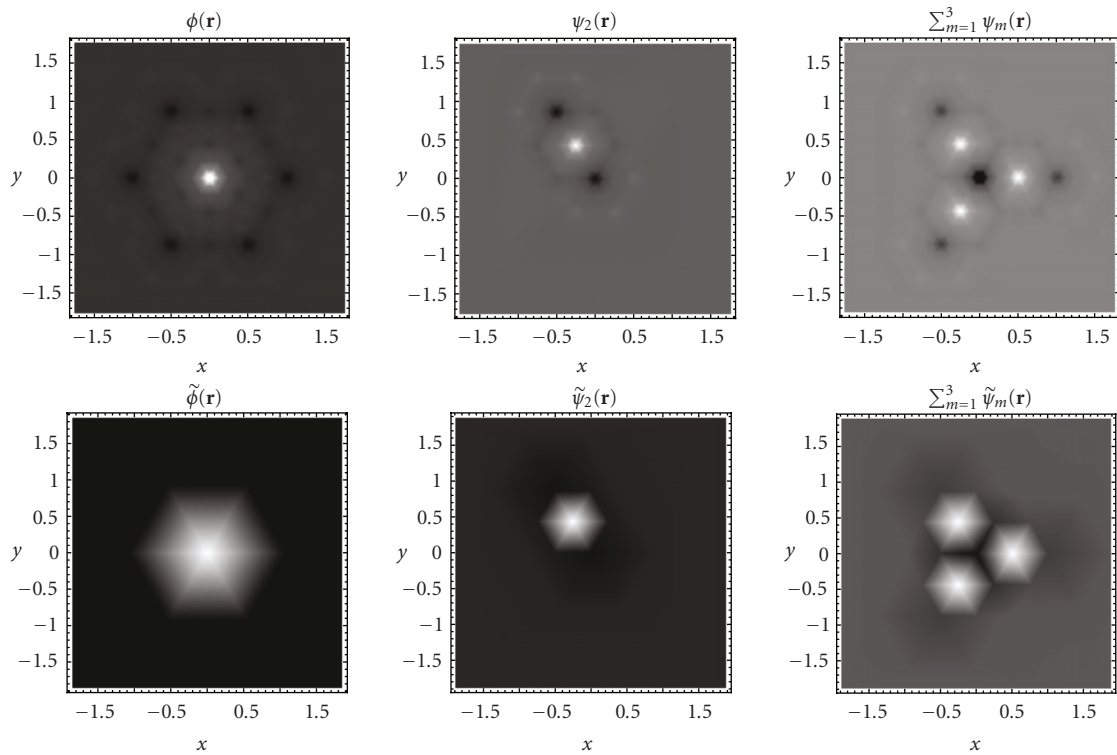
that the second primitive translation vector \mathbf{t}_2 is almost vertical, and then the hexagonal Wigner-Seitz cell approaches a square, as shown in Figure 10. In this limit, the coarse component c_{j-1} and detail components $d_{1,j-1}$, $d_{2,j-1}$, and $d_{3,j-1}$ correspond, respectively, to LL, LH, HL, and HH components of tensor product transform yielded from following the combinations of one-dimensional separable filters

$$\hat{h}(\xi)\hat{h}(\eta), \quad \hat{h}(\xi)\hat{g}(\eta), \quad \hat{g}(\xi)\hat{h}(\eta), \quad \hat{g}(\xi)\hat{g}(\eta), \quad \boldsymbol{\omega} = (\xi, \eta), \quad (63)$$

where (ξ, η) is the rectangular coordinates of $\boldsymbol{\omega}$.



(a) Haar



(b) (2,2) interpolating

FIGURE 9: The density plots of triangular biorthogonal wavelet bases. Each column gives the scaling functions, wavelets in case $m = 2$, and sum of three wavelets from the left. The other wavelets for $m = 1$ and 3 cases are defined by rotating them by $\pm 2\pi/3$ on the plane \mathbb{R}^2 .

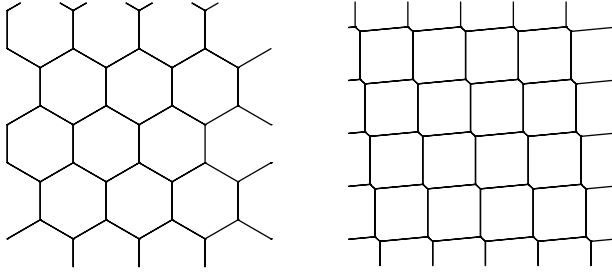


FIGURE 10: Honeycomb and nearly square array of Wigner-Seitz cell.

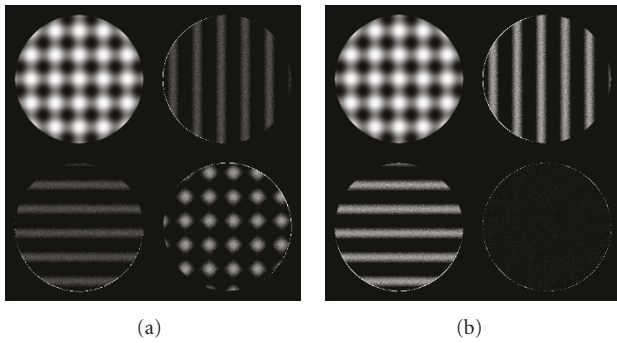


FIGURE 11: Decomposed images of Mesh-circle with triangular Haar (a) and tensorial Haar (b).

The images obtained by the decomposition are displayed in the pyramidal tiling, with the coarse approximation at the top left corner, while the detail components $d_{1_{j-1}}$, $d_{3_{j-1}}$, and $d_{2_{j-1}}$ are arranged clockwise. The grayscale images used here have 512×512 pixels, and we treat the image data as the original signal $\{c_9[\mathbf{t}]\}_{\mathbf{t} \in \Lambda}$ to which the decomposition algorithm is applied with periodic boundary condition in both \mathbf{t}_1 and \mathbf{t}_2 directions.

In a variety of the triangular wavelet filters, we use the Haar and (2,2) interpolating filters constructed in Section 3 as well as their conventional tensor product forms to make the comparison simple. Since the filters are biorthogonal, we assume the L^1 norm of coarse and detail components as the energy.

4.2. Image Decomposition. Let us first discuss the decomposed images of a simple symmetric artificial figure, the Mesh-circle, by one-level decompositions with the triangular Haar filters and their conventional tensor product forms shown in Figure 11. The original image c_9 has been decomposed into a coarse approximation c_8 and three oriented detail components $d_{m,8}$, $m = 1, 2, 3$, with half a resolution, respectively.

Here we can clearly see the three detail components in the triangular decomposition as we expected, while the diagonal detail component $d_{3,8}$ in the tensor product case is not visually apparent. This corresponds to their energy distributions of three detail components which, together with the results of Lena, are shown in Figure 12. As is obvious from the decomposed images of each triangular and

tensor product case for Mesh-circle, d_1 and d_2 components share almost the same amount of energy, implying that the image contains the same density of energy in vertical and horizontal directions. However, diagonal d_3 components are significantly different. Since d_3 component obtained from the tensor product transform is not an independent component, its energy is appreciably less than the other components d_1 and d_2 . In contrast, the triangular case has more energy of d_3 component that is independent and thus the energy is evenly distributed over the three detail components. Note that the Mesh-circle image originally contains diagonal information the most.

In the case of a more realistic image, Lena, the observations are very similar, except for the effect of the directional property, which has the strong energy concentration of d_1 component. Thus isotropy, or rotational invariance, of the original images is well respected in the triangular decomposition.

4.3. Compression. We reconstructed images keeping some of the largest detail components $|d_{m,j}[\mathbf{t}]|$, $j = 8, \dots, 2$, and $|c_2[\mathbf{t}]|$, using both (2,2) interpolating filters. Figure 13 shows compressed images of Lena at the largest 5% of coefficients and their zooms. Since the triangular filters preserve isotropy of an image, they should still represent its edge structures nicely even if the image is compressed. While the triangular case appears to be better at some particular parts of the figures such as the hat of Lena and the frame of the mirror, one might say, however, that the tensorial case has good quality because its Peak-Signal to Noise Ratio (PSNR) value is slightly higher compared with ours. This is due to the fact that the tensor product transform has relatively smaller total energy of detail components. We have observed that the triangular decomposition produces even energy of three detail components while the tensor product case has much less energy of diagonal detail components and thus the total energy is lower. The difference is fairly small but in general causes the serious disadvantage in compression.

The uniform distribution of coefficients is somewhat inconvenient for image compression because in general it needs a biased distribution of coefficients to reduce the entropy. However, for both images shown in Figure 13, we emphasize that no definite statement can be made as to which is better judging from the PSNR values. PSNR is one of the standard criteria of distortion measure, but it does not always agree well with human perception. Nevertheless, the difficulty lies in evaluating the distortion that we actually perceive.

4.4. Edge Detection. The particular property of isotropic energy distributions is very effective when representing the edge of figures. After the one-level decomposition by both sets of Haar filters, we reconstructed images, the Fingerprint and the Boat, only using detail components so that the whole edge structure is detected. Results are shown in Figure 14. In the triangular decomposition for both images, we see that the edge structures of the images are distinctly detected in independent orientations. This is a sharp contrast to the

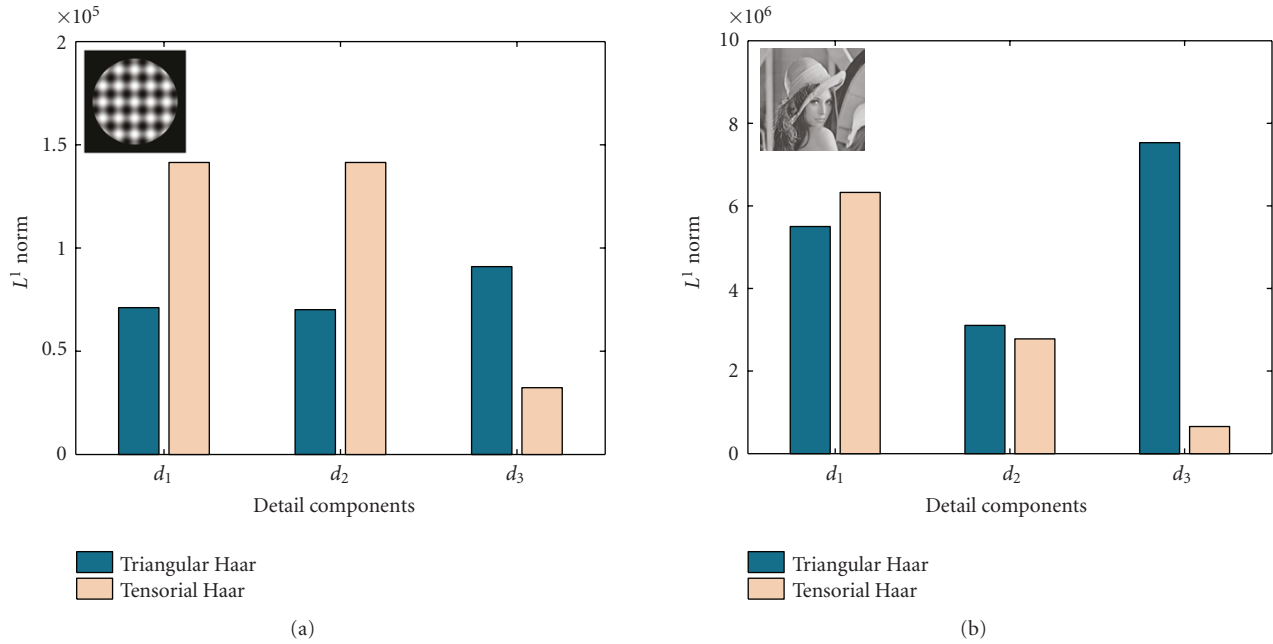


FIGURE 12: Energy (L^1 norm) distributions of three detail components after one-level decompositions for Mesh-circle (a) and Lena (b).



FIGURE 13: Lena reconstructed with the largest 5% of coefficients and its zoom. (a) displays original image, and (b) and (c) show triangular (2,2) case and tensorial (2,2) case having PSNR = 34.4 dB and = 35.5 dB, respectively.

tensorial case, where some parts of the edge information are lost and ringing effects are observed.

The Fingerprint image mainly contains the correlation in the diagonal direction, which is similar to the Mesh-circle because a fingerprint has a spiral structure. Hence, in the triangular decomposition the energy of detail components

should be evenly distributed while most of the energy goes to horizontal and vertical directions in the tensorial one. The reconstruction of the image from only detail components in the triangular case therefore reproduces its edge structures clearly. This might be even more evident in the Boat image. The Boat contains much information composed of straight

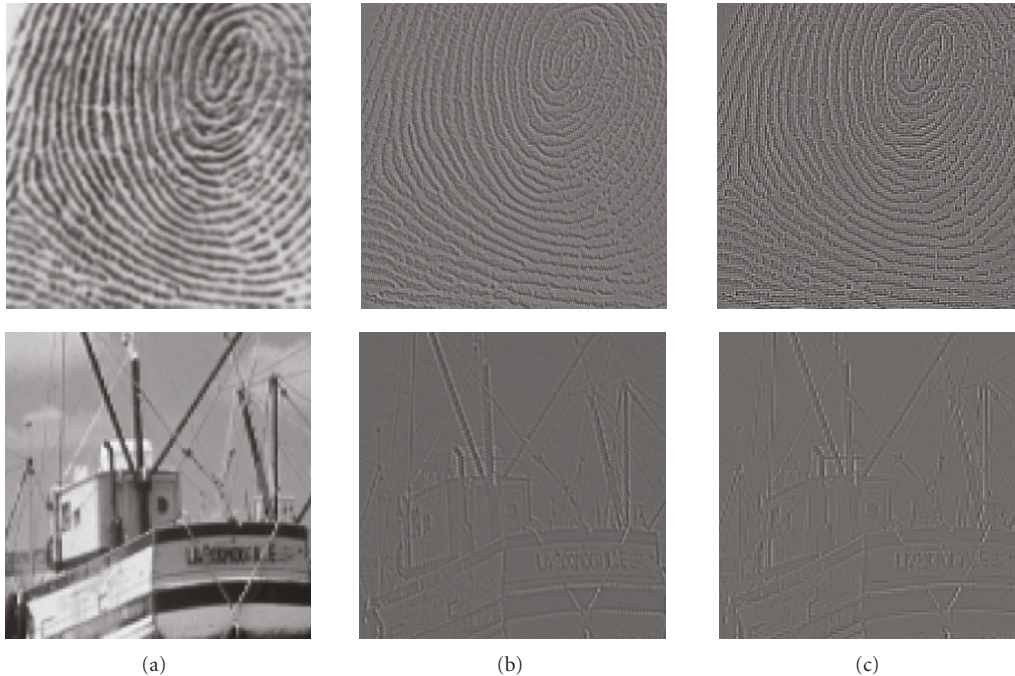


FIGURE 14: Zoom of images reconstructed with only detail coefficients $d_{8,m}$, $m = 1, 2, 3$; each column shows original image, triangular Haar case, and tensorial Haar case from the left.

lines such as masts, which are not clearly represented in the tensor product example. This is true especially for the inclined objects.

These results clearly indicate that for the edge detection it would be more desirable to use the triangular filters as they allow an isotropic image representation. It is also suggestive that our filters are effective for the feature or keypoint detection [30], where isotropy and orientation analysis play an important role.

5. Concluding Remarks

We have developed the nonseparable biorthogonal wavelets on triangular lattice by extending the one-dimensional interpolating wavelets. It turned out that it is possible to design three oriented wavelets having an arbitrary order of vanishing moments. The three HP filters are symmetrically arranged on the lattice thereby allowing them to be isotropic filters and thus giving hexagonal symmetry to the LP filters. Since our formalism is basically a straightforward generalization of the one-dimensional case, the extension to three or multidimension appears to pose no fundamental problems.

In the exploration of effective application examples with triangular wavelet filters in image processing, we have observed that triangular filters have distinctive advantages in the edge detection for independent orientations of images compared to the conventional tensor product forms. This surely suggests that the triangular wavelets are promising in preserving isotropy of images well.

In dealing with more complicated applications such as feature or keypoint detection, the triangular wavelets appear

to be appealing as it can offer the isotropic image processing. We believe the triangular wavelets developed in this paper would be appreciably useful for a wide range of scientific fields, where symmetry plays an important role.

Acknowledgments

This paper is dedicated to the memory of Professor Susumu Sakakibara, who initiated this work but suddenly passed away in May, 2007. The authors are grateful to the referees for valuable remarks and suggestions that have greatly improved the clarity and conciseness of the presentation. K. Fujinoki would like to thank T. Endo for fruitful discussions and Y. Inoue for his help.

References

- [1] S. Mallat, *A Wavelet Tour of Signal Processing*, Academic Press, New York, NY, USA, 2nd edition, 2001.
- [2] A. Cohen and I. Daubechies, "Non-separable bidimensional wavelet bases," *Revista Matemaica Iberoamericana*, vol. 9, no. 1, pp. 51–137, 1993.
- [3] J. Kovačević and M. Vetterli, "Nonseparable multidimensional perfect reconstruction filter banks and wavelet bases for \mathbb{R}^n ," *IEEE Transactions on Information Theory*, vol. 38, no. 2, pp. 533–555, 1992.
- [4] Z. Zhang, H. Fujiwara, H. Toda, and H. Kawabata, "A new complex wavelet transform by using RI-spline wavelet," in *Proceedings of the IEEE International Conference on Acoustics, Speech, and Signal Processing (ICASSP '04)*, vol. 2, pp. 937–940, Montreal, Canada, May 2004.
- [5] N. Kingsbury, "The dual-tree complex wavelet transform: a new technique for shift invariance and directional filters," in

- Proceedings of the 8th IEEE Digital Signal Processing Workshop (DSP '98)*, Bryce Canyon, Utah, USA, 1998, paper no. 86.
- [6] M. Lounsbury, T. D. DeRose, and J. Warren, "Multiresolution analysis for surfaces of arbitrary topological type," *ACM Transactions on Graphics*, vol. 16, no. 1, pp. 34–73, 1998.
- [7] G.-P. Bonneau, "Optimal triangular Haar bases for spherical data," in *Proceedings of the 10th IEEE Visualization Conference (VIS '99)*, pp. 279–284, 1999.
- [8] W. Sweldens, "The lifting scheme: a custom-design construction of biorthogonal wavelets," *Applied and Computational Harmonic Analysis*, vol. 3, no. 2, pp. 186–200, 1996.
- [9] W. Sweldens, "The lifting scheme: a construction of second generation wavelets," *SIAM Journal on Mathematical Analysis*, vol. 29, no. 2, pp. 511–546, 1998.
- [10] P. Schröder and W. Sweldens, "Spherical wavelets: efficiently representing functions on the sphere," in *Proceedings of the 22nd Annual Conference on Computer Graphics and Interactive Techniques (SIGGRAPH '95)*, pp. 161–172, 1995.
- [11] I. Daubechies, I. Guskov, P. Schröder, and W. Sweldens, "Wavelets on irregular point sets," *Philosophical Transactions of the Royal Society A*, vol. 357, no. 1760, pp. 2397–2413, 1999.
- [12] S. Sakakibara and O. V. Vasilyev, "Construction of triangular biorthogonal wavelet filters for isotropic image processing," in *Proceedings of the 14th European Signal Processing Conference (EUSIPCO '06)*, Florence, Italy, September 2006.
- [13] K. Fujinoki and S. Sakakibara, "Properties of triangular wavelet transform on images," *Journal of Signal Processing*, vol. 10, no. 4, pp. 263–266, 2006.
- [14] M. J. D. Powell, *Approximation Theory and Methods*, Cambridge University Press, Cambridge, UK, 1981.
- [15] W. Sweldens and P. Schröder, "Building your own wavelets at home," in *Proceedings of the 23rd Annual Conference on Computer Graphics*, ACM SIGGRAPH Course Notes, pp. 15–87, 1996.
- [16] I. Daubechies, "Orthogonal basis of compactly supported wavelets," *Communications on Pure and Applied Mathematics*, vol. 41, no. 7, pp. 909–996, 1988.
- [17] A. Cohen and J.-M. Schlenker, "Compactly supported bidimensional wavelet bases with hexagonal symmetry," *Constructive Approximation*, vol. 9, no. 2-3, pp. 209–236, 1993.
- [18] E. P. Simoncelli and E. H. Adelson, "Non-separable extensions of quadrature mirror filters to multiple dimensions," *Proceedings of the IEEE*, vol. 78, no. 4, pp. 652–664, 1990.
- [19] E. P. Simoncelli, W. T. Freeman, E. H. Adelson, and D. J. Heeger, "Shiftable multiscale transforms," *IEEE Transactions on Information Theory*, vol. 38, no. 2, pp. 587–607, 1992.
- [20] A. Cohen, I. Daubechies, and J. Feauveau, "Biorthogonal bases of compactly supported wavelets," *Communications on Pure and Applied Mathematics*, vol. 45, no. 5, pp. 486–560, 1992.
- [21] I. Daubechies and W. Sweldens, "Factoring wavelet transforms into lifting steps," *Journal of Fourier Analysis and Applications*, vol. 4, no. 3, pp. 247–269, 1998.
- [22] R. Ansari, C. Guillemot, and J. F. Kaiser, "Wavelet construction using Lagrange halfband filters," *IEEE Transactions on Circuits and Systems*, vol. 38, no. 9, pp. 1116–1118, 1991.
- [23] G. Deslauriers and S. Dubuc, "Symmetric iterative interpolation processes," *Constructive Approximation*, vol. 5, pp. 49–68, 1989.
- [24] S. Dubuc, "Interpolation through an iterative scheme," *Journal of Mathematical Analysis and Applications*, vol. 114, no. 1, pp. 185–204, 1986.
- [25] A. R. Calderbank, I. Daubechies, W. Sweldens, and B.-L. Yeo, "Wavelet transforms that map integers to integers," *Applied and Computational Harmonic Analysis*, vol. 5, no. 3, pp. 332–369, 1998.
- [26] G. Grosso and G. P. Parravicini, *Solid State Physics*, Academic Press, New York, NY, USA, 2000.
- [27] S. G. Mallat, "A theory for multiresolution signal decomposition: the wavelet representation," *IEEE Transactions on Pattern Analysis and Machine Intelligence*, vol. 11, no. 7, pp. 674–693, 1989.
- [28] J. Kovačević and W. Sweldens, "Wavelet families of increasing order in arbitrary dimensions," *IEEE Transactions on Image Processing*, vol. 9, no. 3, pp. 480–496, 2000.
- [29] K. Gröchenig and W. R. Madych, "Multiresolution analysis, Haar bases, and self-similar tilings of R^n ," *IEEE Transactions on Information Theory*, vol. 38, no. 2, pp. 556–568, 1992.
- [30] D. G. Lowe, "Distinctive image features from scale-invariant keypoints," *International Journal of Computer Vision*, vol. 60, no. 2, pp. 91–110, 2004.